Supplementary Information

Independent Control of Mode Selection and Power Extraction in Terahertz Semiconductor Lasers

Kai Wang[1,2], Hongzhou Bai[2,3], Chenren Yu[2,3], Haiqing Zhu[2,3], Pingping Chen[4], Wei Lu[4], Lianhe Li[5], A.Giles Davies[5], Edmund H. Linfield[5], Hua Li[6], Juncheng Cao[6], Chong Chen[7], Harvey E. Beere[7], David A. Ritchie[7] , Li He[2], Gangyi Xu[1,2,*]

1) *Hangzhou Institute for Advanced Study, University of Chinese Academy of Sciences, Hangzhou 310024, China*

2) *Key Laboratory of Infrared Imaging Materials and Detectors, Shanghai Institute of Technical Physics, Chinese Academy of Sciences, Shanghai 200083, China*

3) *University of Chinese Academy of Sciences, Beijing 100049, China.*

4) *National Laboratory of Infrared Physics, Shanghai Institute of Technical Physics, Chinese Academy of Sciences, Shanghai 200083, China*

5) *School of Electronic and Electrical Engineering, University of Leeds, Leeds LS2 9JT, UK.*

6) *Key Laboratory of Terahertz Solid State Technology, Shanghai Institute of Microsystem and Information Technology, Chinese Academy of Sciences, Shanghai 200050, China*

7) *Cavendish Laboratory, University of Cambridge, Cambridge CB3 0HE, UK.*

* email: gangyi.xu@mail.sitp.ac.cn

Content

There are 17 pages and 13 figures in the Supplementary Information.

S1. Role of the absorbing boundaries.

S2. Influence of Q-factor of the ADBR on the mode selection of the THz-ADBR-QCL.

S3. A THz-ADBR-QCL device operating under different bias conditions.

S4. Radiation loss of the grating coupler (GC).

S5. Performances of THz-ADBR-GC-QCL devices with different cavity lengths.

S6. Influence of Λ_{ADBR} on the emitting wavelength of the THz-ADBR-GC-QCL.

S7. Simulation of the far-field beam of the THz-ADBR-GC-QCL.

S8. Experimental approach to determine the reflectivity of the ADBR.

S9. THz-ADBR-GC-QCLs operating at 3.2 - 3.4 THz.

S1. Role of the absorbing boundaries

The absorbing boundaries are composed by the highly doped n$^+$ GaAs (doping concentration 3.5×10^{18} cm^{-3}, 200nm in thickness) top contact layer that is not covered by the top metallization. According to the Drude model, the complex refraction index of this n$^+$ GaAs layer is 5.23 + 19.97i (at 2.9 THz), exhibiting the metallic optical characteristic with very high loss.

The absorbing boundary located in between the ADBR and the left facet is utilized to perfectly absorb the THz wave that transmits through the ADBR. When the electric field transmits through the ADBR and propagates into the absorbing boundary, the calculated reflectivity is as low as 0.2% and the field propagated into the absorbing boundary is quickly annihilated. As a result, once the THz wave transmits through the ADBR, it will be perfectly absorbed and this is very important to build up stable mode oscillation in the whole device. Figure S1 (a) shows the schematic cross-section (in xz-plane) of the absorbing boundary in between the ADBR and the left facet. Figure S1 (b) shows the field profile (E_z) when the THz wave is injected into the absorbing boundary.
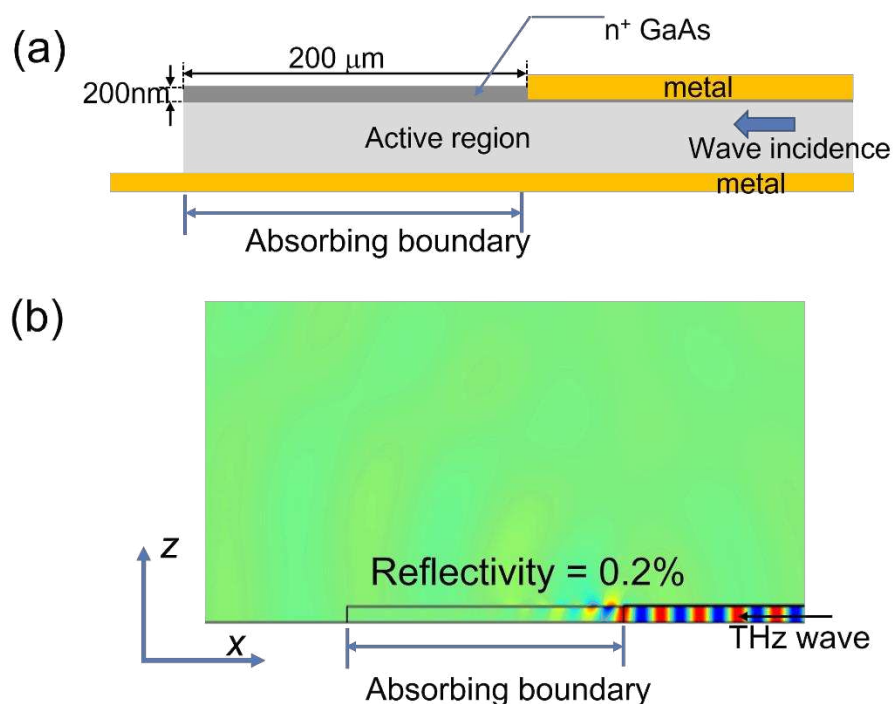

Figure S1. (a) Scheme and structural parameters of the absorbing boundary in between the ADBR and the left facet. (b) The calculated field profile (E_z) when the THz wave transmits through the ADBR and injects into the absorbing boundary. The calculated reflectivity is as low as 0.2%.

The absorbing boundaries located on both lateral sides of the ridge are utilized to eliminate the high order transverse modes. Figure S2 (a) shows the schematic cross-section (in yz-plane) of the ridge, where the structural parameters of the absorbing boundary are given. Figure S2(b) presents the field profiles of the fundamental and the first two high order transverse modes. The waveguide losses of the fundamental, the first-order and the second-order transverse mode are respectively 17.0 cm^{-1}, 21.0 cm^{-1} and 26.8 cm^{-1}. Such difference is sufficient to eliminate the high order transverse modes. From the measurement results of the laser spectra and far field beam pattern, we did not observe the high order transverse mode. In fact, in our previous work of THz DFB lasers and THz master-oscillator power-amplifier (MOPA) lasers (see Refs. 14, 34 and 35 in the main text), the same absorbing boundaries were used which enabled the devices to operate on the fundamental mode.
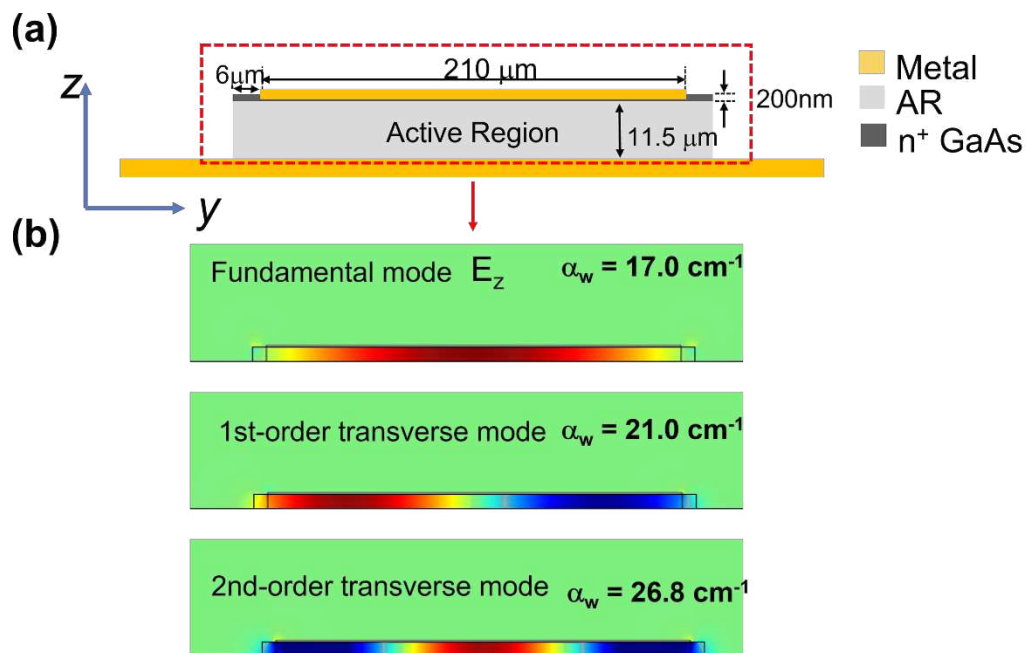

Figure S2: (a) Schematic cross-section (in yz-plane) of the device and the related parameters. (b) Distribution of electric field (Ez) for the fundamental, the first-order and the second-order transverse mode. The calculated waveguide losses (α_w) are also marked.

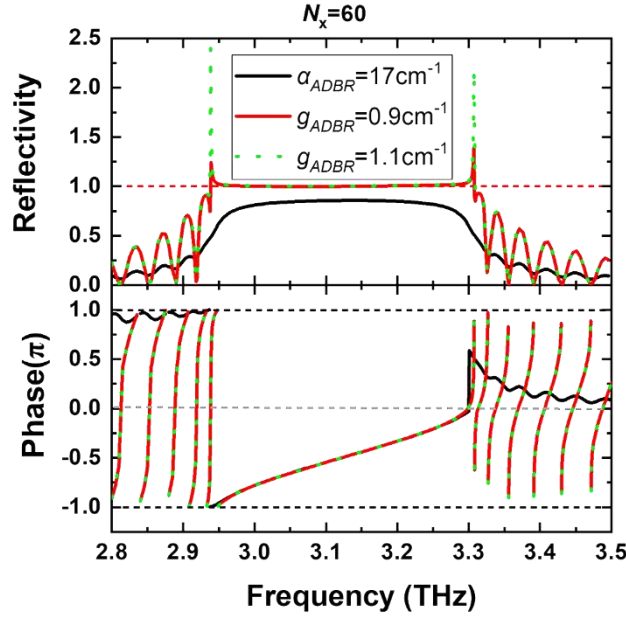## S2. Influence of Q-factor of the ADBR on the mode selection of the THz-ADBR-QCL

Figure S3. Calculated spectra of the reflectivity and reflection phase for the ADBR when the net gain (g) is respectively -17, 0.9 and 1.1 cm^{-1}. For the 2D PhC in the ADBR section, Λ_{ADBR} = 13.9 μm, r = 5.0 μm, and Nx = 60.
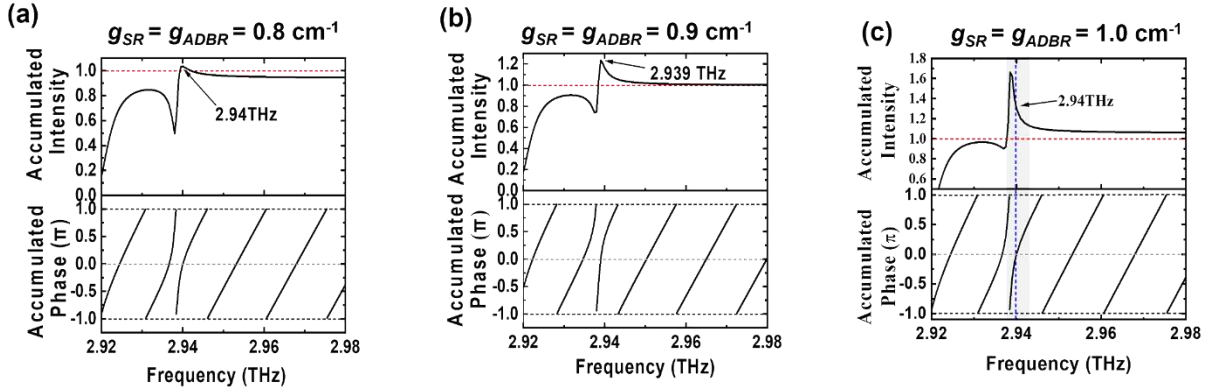
Figure S4. Calculated round-trip accumulated intensity and phase of a THz-ADBR-QCL when the net gain of the cavity is uniformly set as 0.8 cm^{-1} (a), 0.9 cm^{-1}, and 1.0 cm^{-1} (c). The structure parameters of the device are: Λ_{ADBR}= 13.9 μm, N_x = 60, N_y = 14, L_{SR}= 2000 μm.

We consider a THz-ADBR-QCL with N_x = 60, for which the Q-factor of the ADBR is 464, and the necessary net gain for the ADBR to self-lasing is 4.8 cm^{-1}. For this device, Figure S3 shows the spectra of the reflectivity and the reflection phase of the ADBR with different values of net gain (g). Figure S4 shows the evolution of the accumulated intensity and phase after one round trip when g in the whole cavity uniformly increases. When g = 0.8

cm^{-1}, as shown in Fig. S4(a), the intensity condition of laser threshold is satisfied for the candidate modes in the frequency range near the photonic band-edge. However, since the frequency range is so narrow, the phase condition may not be satisfied given the uncertainty of the cavity length. The situation changes when the net gain slightly increases to 0.9 cm^{-1} or 1.0 cm^{-1}, as shown in Figs. S4(b) and S4(c), where in the band-edge region the accumulated intensity exceeds 1 and the accumulated phase covers roughly 2π. The simulations suggest that, when the Q-factor of the ADBR is sufficiently high, the THz-ADBR-QCL device will directly operate in single mode.

The situation will be very different when the ADBR features a low Q-factor. For a THz-ADBR-QCL with $N_x = 20$, the Q-factor of the ADBR is 55, and the necessary net gain for the ADBR to self-lasing is 40.3 cm^{-1}. For this device, Figure S5 shows the spectra of reflectivity and reflection phase of the ADBR with different values of net gain. Fig. S6 shows the accumulated intensity and phase of the possible modes as a function of frequency at different levels of the net gain. Even when the net gain is 6 cm^{-1}, no reflection peak of the ADBR appears and there are several modes in the photonic band gap of the ADBR that match the laser threshold conditions. It suggests that multimode operation is expected for a THz-ADBR-QCL with a low-Q ADBR.
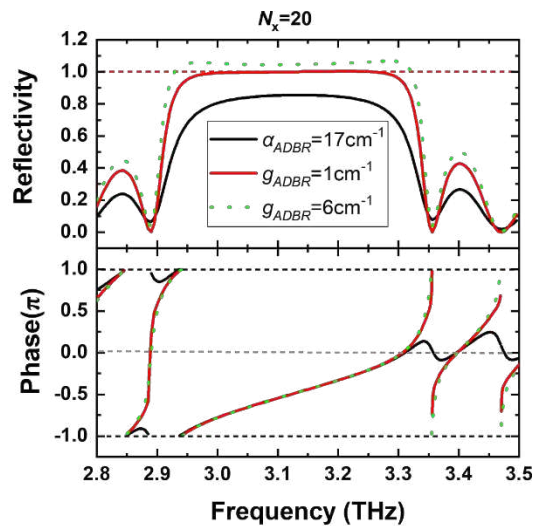
Figure S5. Calculated spectra of the reflectivity and reflection phase for the ADBR when the net gain (g) is respectively -17, 1.0 and 6.0 cm^{-1}. For the 2D PhC in the ADBR section, Λ_{ADBR} = 13.9 μm, r = 5.0 μm, and Nx = 20.
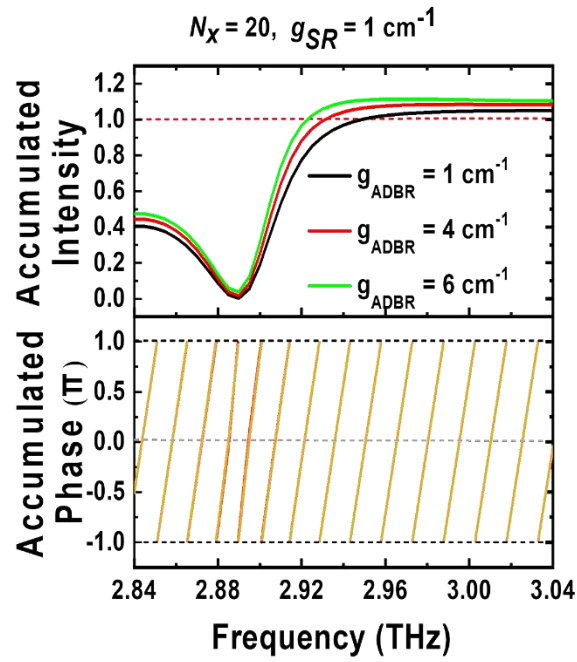
Figure S6. Calculated round-trip accumulated intensity and phase of a THz-ADBR-QCL device (N_x=20) at different levels of net gain. The structure parameters, except N_x, are the same as those in Figure S4.

S3. THz-ADBR-QCL operating under different bias conditions.
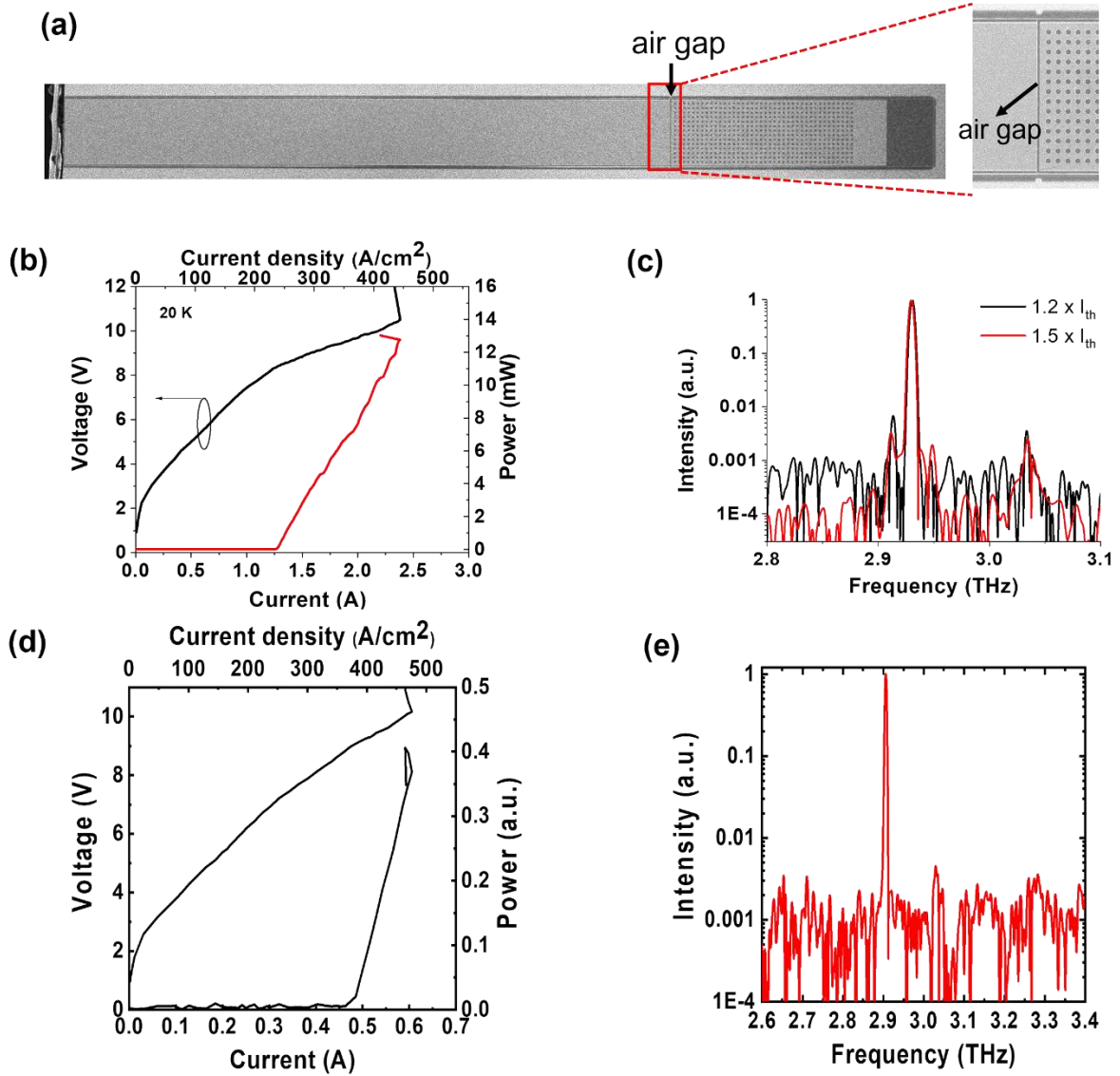
Figure S7. (a) SEM images of a THz-ADBR-QCL, where an air gap in the top metalization seperating the ADBR and the SR. In the ADBR section, Λ_{ADBR} = 13.9 µm, r = 5.0 µm, N_x = 40, N_y =14. In the SR section, L_{SR} = 2000 µm. Panels (b) and (c) show the L-I-V curves and the emission spectra when the whole device is uniformly biased. Panels (d) and (e) show the L-I-V curves and the emission spectrum of the device when only the ADBR is biased. The device was measured in pulsed mode at 20 K.

In order to experimentally investigate the gain-dependent reflectivity of the ADBR section, we fabricated some THz-ADBR-QCL devices, where in the top metallization the SR and the ADBR are separated by an air gap. Figure S7(a) shows the SEM picture of such a device. The distance between the air gap and the first column of the photonic crystal equals to

Λ_{ADBR}. Such configuration allows the ADBR to be separately biased but avoids disturbing the mode oscillation in the ADBR. For the measured device, the values of N_x, N_y, r, Λ_{ADBR}, L_{SR} and w_{ridge} are respectively 40, 14, 5.0 µm, 13.9 µm, 2000 µm and 210 µm.

Figures S7(b) and S7(c) display the *L-I-V* curves and the emission spectra of the device when both the ADBR and the SR are simultaneously biased, measured in pulsed mode at 20 K. The device operates in single mode, and the threshold current is 233 A/cm^2. Figure S7(d) displays the *L-I-V* curves of the device where only the ADBR section is biased, measured at 20 K. The results reveal that the ADBR does self lase but with a threshold current density of 355 A/cm^2, which is remarkably higher than that of the device where both the SR and the ADBR are simultaneously biased. Figure S7(e) shows the spectrum of the self-lasing mode of the ADBR when the output power reaches to its maximum. The emission frequency is 2.91 THz, corresponding to the band-edge mode of the ADBR (shown in Figure 1(b) of the main text). The reason of single-mode emission is that the low-frequency band edge mode aligns with the gain peak, and this is also the reason that the reflectivity peak caused by the low-frequency band-edge is utilized in this work. The high threshold of self-lasing indicates that the ADBR should not be regarded as a seed laser, but rather a mirror with high reflectivity and extremely narrow bandwidth.
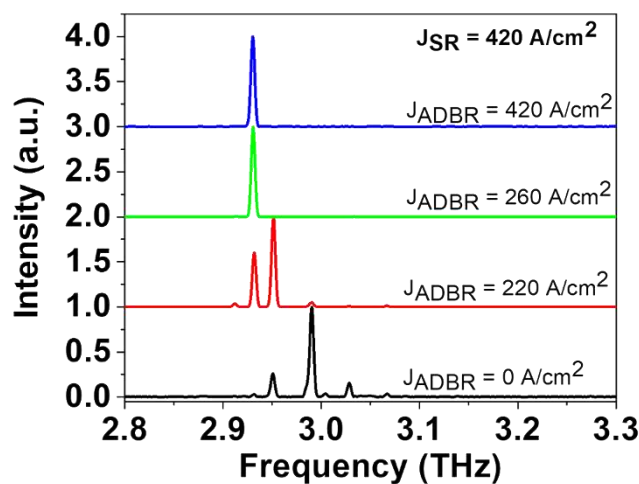
Figure S8. Laser spectra when the ADBR and the SR are seperately biased. Here the current density of the SR (J_{SR}) is fixed at 420 A/cm^2, and the current density of the ADBR (J_{ADBR}) varies from 0 to 420 A/cm^2.

Then, we separately biased the SR and the ADBR by two pulse generators, and the two trains of current pulses were synchronized by using the trig mode. The injected current density of the SR was fixed at the level of maximum output (J_{SR} = 420 A/cm^2) while the

current density of the ADBR (J_{ADBR}) varied from 0 to 420 A/cm^2, and the emission spectra are shown in Figure S8. When $J_{ADBR} = 0$, the device operates in multimode whose frequencies locate in the photonic band gap of the ADBR. When $J_{ADBR} = 220$ A/cm^2 which is less than the threshold current density (233 A/cm^2) shown in Fig. S7(b), the device still shows multimode emission. When $J_{ADBR} = 260$ A/cm^2 ($\sim 1.1 \times J_{th}$) and $J_{ADBR} = 420$ A/cm^2 ($\sim 1.8 \times J_{th}$), the device exhibits single mode emission with the lasing frequency in consistent with that shown in Fig. S7(c). Note, in this proceeding, J_{SR} is fixed at the maximum value. It unambiguously illustrates that g_{ADBR} is not clamped by the band gap modes. Instead, g_{ADBR} grows until the narrow reflection peak appears and forces the device to operate on the band-edge mode.

S4. Radiation loss of the grating coupler (GC)

When the THz wave propagates along the grating coupler (GC), part of it will be radiated into the free space and therefore the intensity of the wave decays along the GC. From the decay we can deduce the radiation loss (α_{GC}) of the GC. Figure S9(a) shows schematically the 2D cross-section used to calculate α_{GC}, and Figure S9(b) shows the propagation and radiation of the THz wave after it is injected into the GC. The inset of Figure S9(b) shows the decay of the time-averaged Poynting vector (Px) along the center line of the GC e, from which α_{GC} is found to be 50 cm^{-1}.

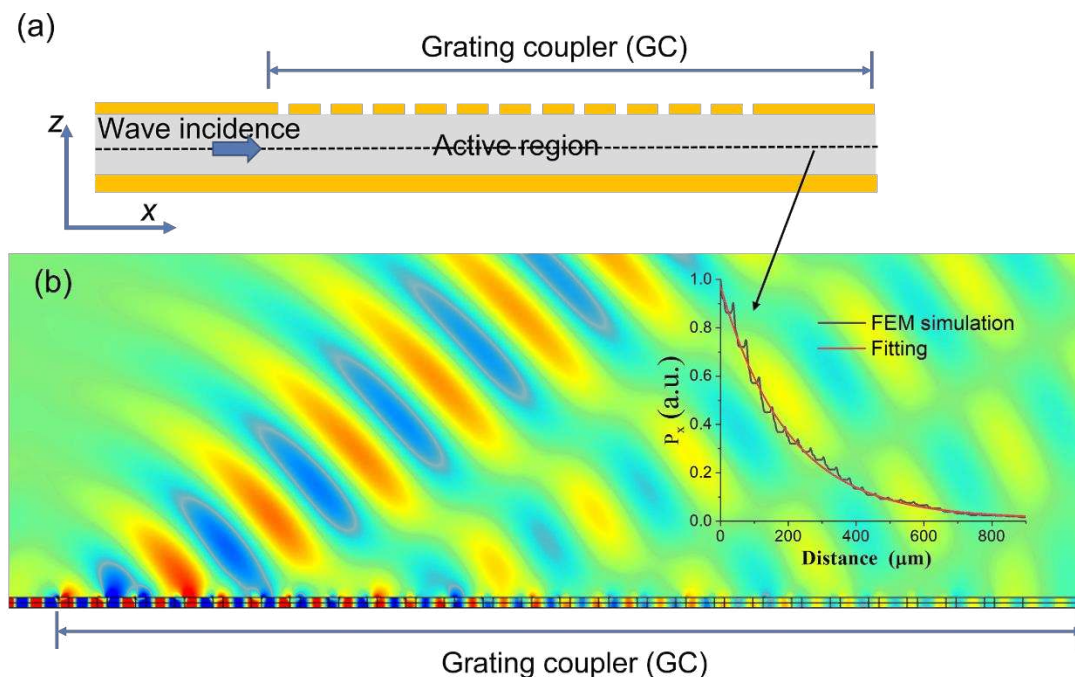
Figure S9. (a) Schematic cross-section (x-z plane) of the metal-metal waveguide and the GC. (b) Field distribution (E_z) when the THz wave is injected into the GC. The inset of panel (b) shows the decay of Px along the central line of the GC, where the black line corresponds to the simulation result by means of the finite element method and the red curve is the result of exponential fitting.

S5. Performances of THz-ADBR-GC-QCL devices with different cavity lengths.

For the group of the THz-ADBR-GC-QCL devices that described in Fig. 5 of the main text, we have systematically measured the *L-I-V* curves at different operating temperatures as well as the emission spectra at different injected currents at 20K, and the results are presented in Fig. S10. These four devices have the same structure parameters except the L_{ph} which is the distance between the GC and the right cleaved facet, corresponding to different reflection phases of the GC (φ_{GC}). The results show that, despite of the variation of φ_{GC}, the devices have very similar performances in terms of threshold current density, peak output power and maximum operating temperature. The laser spectra show that, except Device D where a few weak side modes are observed, the other devices exhibit single mode emission in most part of the laser dynamic range and the emission frequency corresponds to the low-frequency photonic band-edge. Although it is not available to precisely design the accumulated phase of
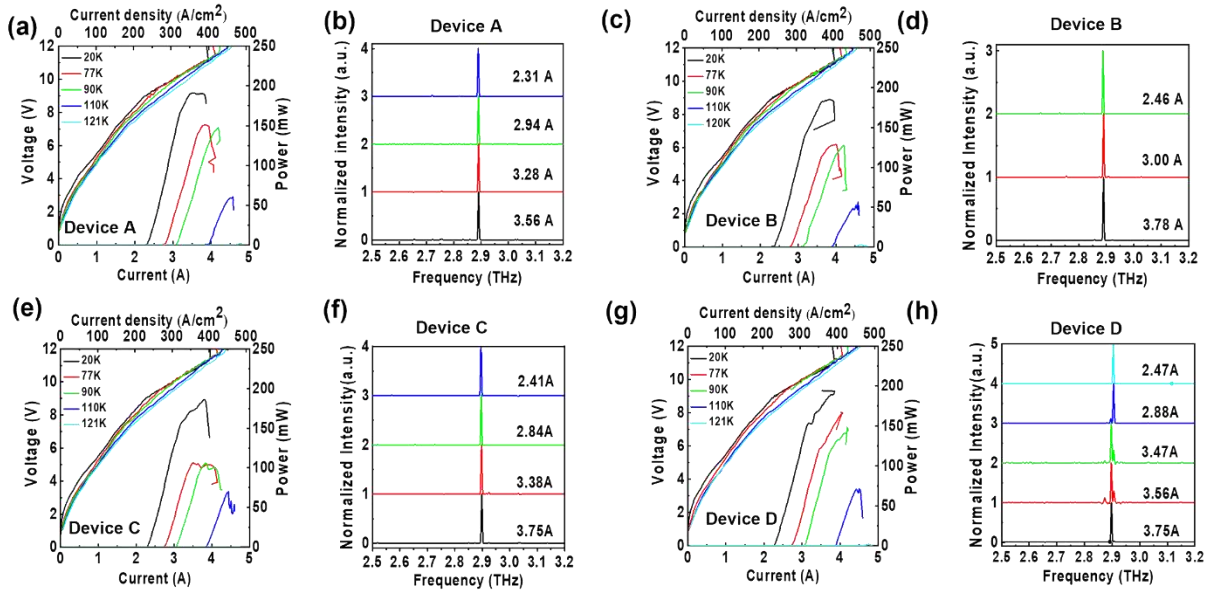

Figure S10. Measured *L-I-V* curves and the emission spectra of a group of THz-ADBR-GC-QCL devices. The only varied structure parameter of these four devices is L_{ph} which is 311.2 µm (Device A), 314.7 µm (Device B), 318.2 µm (Device C), and 321.7 µm (Device D). All the other parameters are fixed as: Λ_{ADBR} = 14.5 µm, r =5.0 µm, N_x = 40, N_y = 14, Λ_{GC} = 38 µm, N_{GC} = 25, x_{slit} = 10 µm, L_{SR}= 3200 µm. The *L-I-V* curves were measured at different operating temperatures, and the laser spectra were measured at 20K at different injected currents, all in pulsed mode. The device number, the operating temperature, and the injected current are marked in the figure.

one round trip because of the uncertainty of cavity length, the THz-ADBR-GC-QCL device can stably operate on single mode. The main reason is that, in the narrow frequency range of the reflectivity peak caused by the ADBR, the round-trip phase covers roughly 2π.

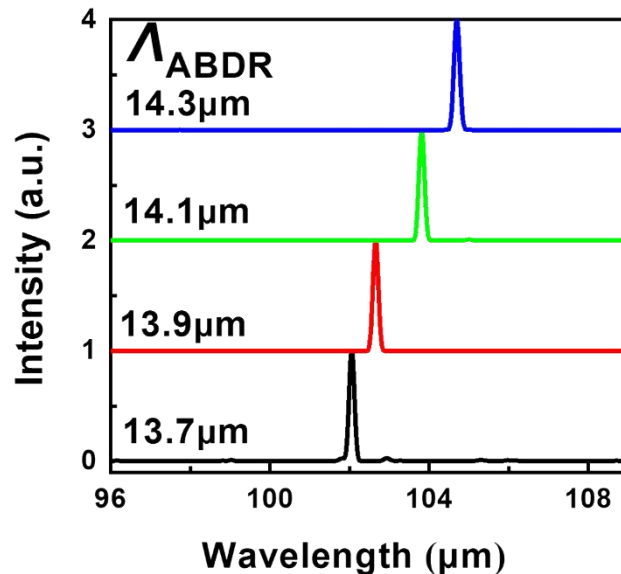**S6. Influence of Λ_{ADBR} on the emitting wavelength of the THz-ADBR-GC-QCLs.**

Figure S11. Emission spectra of 4 THz-ADBR-GC-QCL devices where Λ_{ADBR} varies from 13.7 μm to 14.3 μm. The spectra are recorded near the maximum output at 20 K in pulsed mode. The spectra are shifted vertically for clarity and the values of Λ_{ADBR} are marked in the figure.

In order to investigate the mode section of the ADBR, four THz-ADBR-GC-QCL devices were fabricated where the only varied parameter is Λ_{ADBR} which changes from 13.7 μm to 14.3 μm. The other structure parameters are fixed as: $r = 5.0$ μm, $N_x = 40$, $N_y = 14$, Λ_{GC} = 38 μm, $W_{slit} = 10$ μm and $N_{slit} = 25$. All the devices are ~ 4600 µm × 210 µm in dimension. Figure S11 gives the emission spectra of these 4 devices in pulsed mode at 20K. The results clearly confirm single-mode emission of the devices, and the emission wavelength changes linearly with Λ_{ADBR}. The measurements unambiguously demonstrate that the low-frequency band-edge of the ADBR determines the laser frequency.

S7. Simulation of the far-field beam pattern of the THz-ADBR-GC-QCL.

Figure S12 (a) shows the definition of the angular space during the measurement of far-field beam pattern. Figure S12 (b) shows the simulated beam pattern of a THz-ADBR-GC-QCL device whose structure is the same as that described in the Figure 6 of the main text. To calculate the beam pattern, we first get the electromagnetic field distribution in the near field, i.e., 10 μm above the device surface. Fourier transfer was then carried out to obtain the far-field beam pattern in the angular space, using the procedure described in Refs. [1, 2]. Numerical calculations were conducted by the software COMSOL Multiphysics.
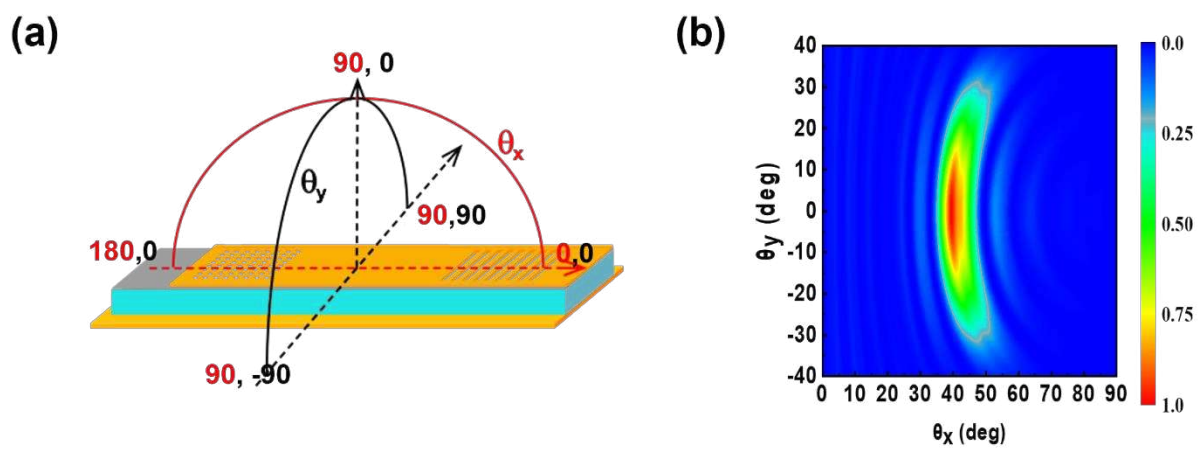

Figure S12. (a) Schematic diagram defining the scanning angles used in beam-profiling measurements. (b) Calculated beam pattern of a THz-ADBR-GC-QCL device whose structure is the same as that described in Figure 6 of the main text.

S8. Experimental approach to determine the reflectivity of the ADBR.

Here, we propose the experimental approach to determine the gain-dependent reflectivity of the ADBR (R_{ADBR}). We assume that, the waveguide loss (α_w) of the devices based on the metal-metal (MM) waveguide is the same and the facet reflectivity (R) of the MM waveguide can be precisely calculated. On these bases, we can first obtain the gain coefficient (G) by measuring the threshold current density (J_{th}) of a series of FP-MM devices with different cavity length. Then, we can measure the threshold of a THz-ADBR-QCL (the length of straight ridge is L_{SR}) and a FP-MM laser (cavity length is L), and we mark their threshold current densities as $J_{th,ADBR}$ and $J_{th,FP}$, respectively. Then we immediately have

$$G \times J_{th,FP} = \frac{1}{2L} \ln \left(\frac{1}{R^2} \right) \qquad \text{for the FP-MM laser} \qquad (1)$$

$$G \times J_{th,ADBR} = \frac{1}{2L_{SR}} \ln \left(\frac{1}{R \times R_{ADBR}} \right) \qquad \text{for the THz-ADBR-QCL} \qquad (2)$$

From equations (1) and (2), we read

$$G \times (J_{th,ADBR} - J_{th,FP}) = \frac{1}{2L_{SR}} \ln \left(\frac{1}{R \times R_{ADBR}} \right) - \frac{1}{2L} \ln \left(\frac{1}{R^2} \right) \qquad (3)$$

Note that the term ($J_{th,ADBR}$ - $J_{th,FP}$) is very necessary, because both $J_{th,ADBR}$ and $J_{th,FP}$ contains the same leakage current components which relate to the electric band structure of the active region. Therefore, the term $G \times (J_{th,ADBR} - J_{th,FP})$ purely reflects the difference of mirror loss between the two lasers. From equation (3) we can deduce the gain-dependent reflectivity of the ADBR.

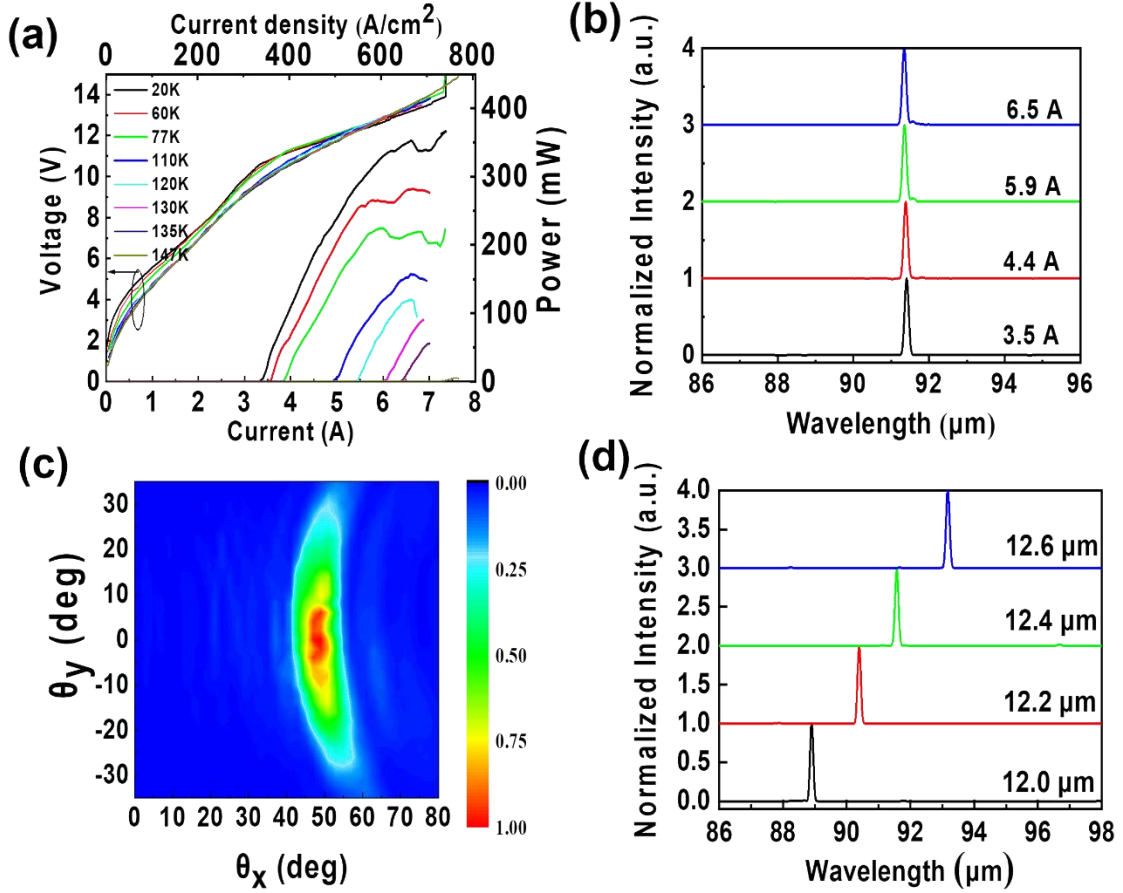## S9. THz-ADBR-GC-QCLs operating at 3.2 - 3.4 THz.

Figure S13. Electrical and optical characterization of the THz-ADBR-GC-QCL devices fabricated with the wafer L1162. Panels (a) – (c) show the results of an optimized device. (a) *L-I-V* curves measured at different operating temperatures. (b) Normalized emission spectra measured at differetn injected currents at 20 K. (c) Measured 2D Far-field beam pattern. (d) Normalized emission spectra of the devices with different Λ_{ADBR} marked in the figure, measured at 20 K.

To confirm the robustness of our concept, here we provide experimental results of the THz-ADBR-GC-QCL devices that operate in the frequency range of 3.2-3.4 THz. The active region of the devices (wafer L1162) is the same as that in Ref. 3. The values of L_{SR} and w_{ridge} are respectively 3200 μm and 210 μm. In the GC section, Λ_{GC}, W_{slit} and N_{slit} are respectively 34 μm, 7 μm and 30. In the ADBR section, r, N_x and N_y are respectively 3.5 μm, 46 and 16. Devices with different values of Λ_{ADBR}, varying from 12.0 μm to 12.6 μm, were investigated. Measurements were conducted in pulsed mode with a repetition rate of 10 kHz and a pulse width of 1 μs.

Figures S13(a) – S13(c) present the measurement results of an optimized device (Λ_{ADBR} =12.4 μm). Figure S13(a) shows the *L-I-V* curves at different operating temperatures. The output power reaches to 366 mW at 20 K and remains 224 mW at 77K, and the maximum operation temperature is up to 147 K. The slope efficiency and wall-plug efficiency were estimated to be 144 mW/A and 0.4%, respectively, at 20 K. Figure S13(b) shows the normalized spectra at different injected currents measured at 20K, illustrating robust single-mode operation in the whole laser dynamic range. Figure 13(c) shows the measured 2D beam pattern at the peak output power, which shows the full-width half-maximum divergence of the emission beam is ~7°×34°. When Λ_{ADBR} changes from 12.0 μm to 12.6 μm, the emission wavelength changes approximately linearly from 88.4 μm to 93.3 μm, as shown in Fig. S13(d), which exemplifies that the lasing mode is decided by the periodicity of the photonic crystal.

References

1 Vuckovic, J.; Loncar, M.; Mabuchi, H.; Scherer, A. Optimization of the Q factor in photonic crystal Microcavities, *IEEE J. Quantum Electron.* **2002**, 38, 850-856.

2 Ryu, H. Y.; Notomi, M.; Lee, Y. H. Finite-difference time-domain investigation of band-edge resonant modes in finite-size two-dimensional photonic crystal slab, *Phys. Rev. B* **2003**, 68, 045209.

3 Li, L.; Chen, L.; Zhu, J.; Freeman, J.; Dean, P.; Valavanis, A.; Davies, A.; Linfield, E. Terahertz quantum cascade lasers with> 1 W output powers. *Electron. Lett*. **2014**, 50, 309-311.